



Optics Letters

Single-shot surface 3D imaging by optical coherence factor

JIAN XU,*  RUIZHI CAO,  MICHELLE CUA, AND CHANGHUEI YANG

Department of Electrical Engineering, California Institute of Technology, Pasadena, California 91125, USA

*Corresponding author: jxxu@caltech.edu

Received 29 November 2019; revised 20 February 2020; accepted 21 February 2020; posted 25 February 2020 (Doc. ID 384551); published 18 March 2020

We report a single-shot three-dimensional (3D) topographical imaging method, optical coherence factor (OCF) imaging, which uses optical coherence as the contrast mechanism to acquire the surface height (z -direction) information of an object. A 4-f imaging system records the light field reflected from the surface of the object. The illumination of the imaging system comes from a laser source with the optical coherence length comparable to the depth of field (DoF) of the optical system. Off-axis holographic recording is used to retrieve the coherence factor from the interference fringes, which is then converted to z -direction information. In this experiment, we validate our 3D imaging results comparing them to axial scanning full-field optical coherence tomography images. We also analyze the contrast mechanism of OCF and show that it is able to provide additional information over conventional coherent and incoherent imaging using the same imaging setup. This single-shot computationally efficient method may have potential applications in industrial quality control inspection. © 2020 Optical Society of America

<https://doi.org/10.1364/OL.384551>

Since real world objects are three dimensional (3D) in nature while common image sensors are two dimensional (2D), optical researchers have worked extensively on different methods to use the captured low dimensional data to reconstruct 3D images. It is worth noting that real world scenes generally consist of multiple surfaces instead of dense 3D voxels, because light usually only interacts with the surface of an object. Under this condition, 3D imaging can be recast as a height-measurement problem (topographic scenarios) and the imaging results are usually topographical in height direction (z -direction).

A variety of methods have been developed to realize 3D imaging from 2D data, including optical coherence tomography (OCT) [1,2], structured light illumination [3], light field cameras [4,5], lensless cameras [6,7] and point spread function (PSF) engineering [8–10]. Some of the 3D imaging methods such as OCT [1,2] inherently reconstruct 3D voxels. For topographic scenarios, these types of 3D imaging methods are generally inefficient as the inherent information in such scenes are much more constrained and lower in magnitude. The other aforementioned methods—from structured light illumination

to PSF engineering—can take advantage of or even rely on the topography condition. Structured light illumination methods [3] usually require a set of spatially varying illumination patterns on the surface of the object, and the height information can be inferred from the distortion of the projected patterns. However, there will be ambiguities in the reconstructed height profile if the object surface has a certain amount of discontinuity. In addition, structured light illumination requires precise calibration before data acquisition. Light field cameras [4,5] are able to capture both 2D space and 2D angle information to realize 3D reconstruction in a single shot, but all of them must trade off space-bandwidth products (effective voxels). Lensless cameras [6,7] replace the conventional image lenses in front of the sensor with an encoding element, such as an amplitude mask or even a random diffuser, and computationally reconstruct the 3D image from the recorded pattern. PSF engineering methods [8–10] implement coded pupils such that objects at different heights have a different PSF on the image sensor. The height information is inferred from the extent of blurring across the scene by computational methods. Both lensless cameras and PSF engineering methods require non-trivial algorithms to reconstruct the height information from the recorded patterns.

On a more fundamental level, these 3D imaging methods can be classified into different categories based on the approach by which they convert height information into detectable signals. OCT encodes the height information to coherence profile, structured light illumination encodes it to pattern distortion, and light field imaging, lensless cameras and PSF engineering methods encode it to the corresponding 2D patterns based on the optical system.

In this Letter, we report a single-shot 3D imaging method, named optical coherence factor (OCF) imaging, which converts the height information into the coherence profile, i.e., different heights provide different coherence factors. We first introduce and explain the OCF imaging approach. Next, we report experimental height reconstruction results from OCF collected with our prototype and show that the results are well matched with images acquired with an axial scanning full field OCT (FFOCT) system. We then demonstrate that OCF is able to provide additional height information than conventional incoherent imaging methods. Finally, we discuss the advantages and tradeoffs of OCF over conventional height reconstruction methods.

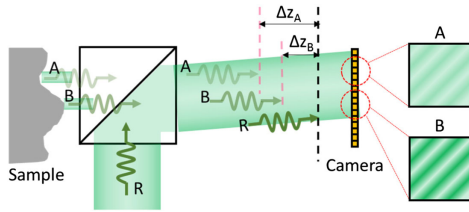


Fig. 1. Working principle of OCF. The reference beam and sample beam with a pathlength difference Δz (Δz_A or Δz_B) will create interference fringes on the camera with the fringe visibility corresponding to Δz . The height information is then inferred from the fringe visibility. Illumination arm for the sample is omitted for simplicity.

Figure 1 shows the working principle of OCF. The sample beam reflected from the sample surface (illumination optics omitted) interferes with a reference beam with a pathlength difference Δz . The interference fringes on the camera have different fringe visibility depending on the pathlength difference: Comparing to part B, part A has more pathlength difference with the reference beam R; therefore, the fringe visibility is lower. Mathematically, we can introduce a coherence factor $\gamma(\Delta z)$ into the interference, and the image on the camera reads as

$$I(\mathbf{r}) = |E_r(\mathbf{r})|^2 + |E_s(\mathbf{r})|^2 + 2\gamma(\Delta z)E_r(\mathbf{r})E_s(\mathbf{r}) \times \cos(\mathbf{k} \cdot \mathbf{r} + \phi_r(\mathbf{r}) - \phi_s(\mathbf{r})), \quad (1)$$

where $\mathbf{r} = (x, y)$ is the pixel location on the camera; \mathbf{k} is the wave vector of the reference beam; E_r , ϕ_r , and E_s , ϕ_s are the amplitudes and phases of the reference beam and sample beam, respectively; and $\gamma(\Delta z)$ is the coherence factor when the pathlength difference is Δz . Equivalently, $\gamma(\Delta z)$ is the coherence profile of the laser (Fig. 2 inset). The form of Eq. (1) makes an assumption that the coherence factor in a local area is a constant. Therefore, the interference term is scaled by the coherence factor. It should be noted that the pathlength difference comes from two sources: (1) height variations from the sample and (2) the relative tilt between the sample beam and reference beam. The former one reflects the spatial information of the sample, while the latter one only adds a slope on the reconstructed height image. Since the incidence angle of the reference beam can be deduced from the periodicity of the interference fringes, we can computationally remove the slope in the height reconstruction. As $\gamma(\Delta z)$ is symmetric with respect to Δz , we set the pathlength difference always positive or negative within the DoF such that the whole field of view (FoV) falls in the monotonic part of the coherence profile. It should be noted that this single shot method relies on the topographical condition, which means that the scenes only consist of surfaces, so that each coherence factor unambiguously maps to one height according to the calibrated coherence profile of the light source (Fig. 2 inset). The quantitative height result can be found from a lookup table of pathlength differences and coherence factors that were previously quantified and tabulated.

The experimental setup of OCF is shown in Fig. 2. The laser beam (532 nm, 150 mW, CrystaLaser Inc. USA) is first split into two arms by a polarizing beam splitter (PBS). Light on arm R1 serves as the reference beam and light on arm R2 illuminates the sample. The sample is imaged onto the camera (GX1920, Allied Vision) by a 4-f system. A tilted plane wave (R1) is added on the

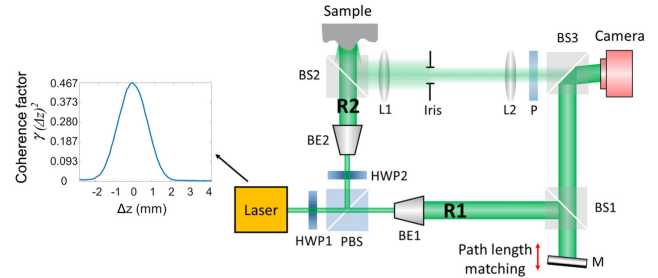


Fig. 2. Schematic of the optical system. BE, beam expander; BS, beam splitter; HWP, half wave plate; L, lens; M, mirror; P, polarizer. Inset: the laser coherence profile with respect to a path length mismatch Δz .

camera by BS3 and interferes with light from arm R1, creating an off-axis hologram on the camera. We perform pathlength difference adjustments on R1 such that (1) the pathlength difference between the two arms is in the monotonic region of the laser coherence profile, and (2) the whole scene in DoF interferes with the reference beam. The coherence factor is retrieved from the hologram by using off-axis holography [11]. The coherence profile of the laser was characterized before imaging experiments. To measure the coherence profile, we put a mirror as the sample, and axially scanned the reference mirror M to acquire multiple frames of interference fringes. A subarea of each frame was analyzed to obtain the coherence factor. The coherence profile in the Fig. 2 inset consists of the correspondence between the coherence factor and pathlength difference.

Since a 4-f system was used to image the sample onto the camera sensor, $E_r(\mathbf{r})$ here is the electric field component of the reference light that is interfering with the sample reflection from location \mathbf{r} on the sample surface. An iris was put on the Fourier plane of the 4-f system such that the spatial frequency components of the DC term $|E_s(\mathbf{r})|^2$ do not overlap with the interference term [third term in Eq. (1)]. The Fourier transform of the captured hologram is shown in Fig. 3 ($F\{I(\mathbf{r})\}$). The central lobe is the Fourier transform of the DC terms $|E_r(\mathbf{r})|^2$ and $|E_s(\mathbf{r})|^2$ [first two terms in Eq. (1)], and the two side lobes are the Fourier transform of the interference term [third term in Eq. (1)]. Since the interference term is separated in Fourier domain with the DC terms, we can crop it out, shift it back to the center, and do inverse Fourier transform to get one copy of the conjugate pair

$$\text{interf}(\mathbf{r}) = E_r(\mathbf{r})E_s(\mathbf{r})\gamma(\Delta z)\exp(-i(\phi_r(\mathbf{r}) - \phi_s(\mathbf{r}))). \quad (2)$$

The coherence factor is calculated by

$$\gamma(\Delta z)^2 = |\text{interf}(\mathbf{r})|^2 / (|E_r(\mathbf{r})|^2|E_s(\mathbf{r})|^2 + \lambda_{\text{reg}}), \quad (3)$$

where λ_{reg} is the regularization term. Theoretically, if we rewrite Eq. (2), we will find λ_{reg} is zero. In practice, to avoid division by zero (this happens when $|E_s(\mathbf{r})|^2$ is approximately zero), λ_{reg} is set to be above the noise level in the hologram measurement. We set λ_{reg} equal to the camera pixel value of 50. In the experiment, the reference beam intensity $|E_r(\mathbf{r})|^2$ is pre-calibrated, and the sample beam intensity $|E_s(\mathbf{r})|^2$ is calculated by subtracting $|E_r(\mathbf{r})|^2$ from the inverse Fourier transform of the central lobe. After getting the coherence factor information $\gamma(\Delta z)^2$, the height value is read from a pre-calibrated laser coherence profile (Fig. 2 inset).

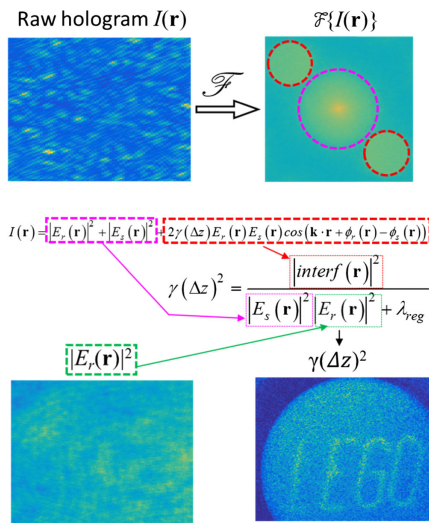


Fig. 3. Flow chart of OCF image processing. The three terms from Eq. (1) are calculated from the hologram (pink and red enclosed boxes) and pre-calibrated reference beam (green box). The coherence factor is then calculated.

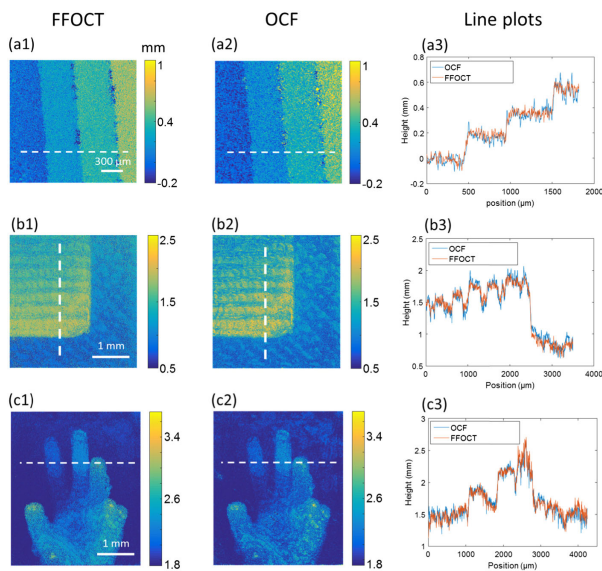


Fig. 4. Quantitative height reconstruction results of (a1)–(c1) FFOCT, (a2)–(c2) OCF, and (a3)–(c3) 1D line plots of the white dashed lines in (a1)–(c1) and (a2)–(c2).

Figure 4 demonstrates the quantitative height reconstruction results of OCF. We stacked pieces of coverslips together in a step shape, where each piece had a thickness of 200 μm . The coverslips were sprayed with white paint to avoid multiple reflections from glass surfaces. The OCF quantitative height reconstruction result of the coverslip stack is present in Fig. 4(a2). An axial scanning FFOCT result serving as ground truth is shown in Fig. 4(a1). For FFOCT, we scanned the reference mirror and took multiple holograms, then determined the height by looking at the maximum interference coherence factor. The OCF and ground-truth FFOCT results are closely matched with each other, as exhibited in the line plot Fig. 4(a3).

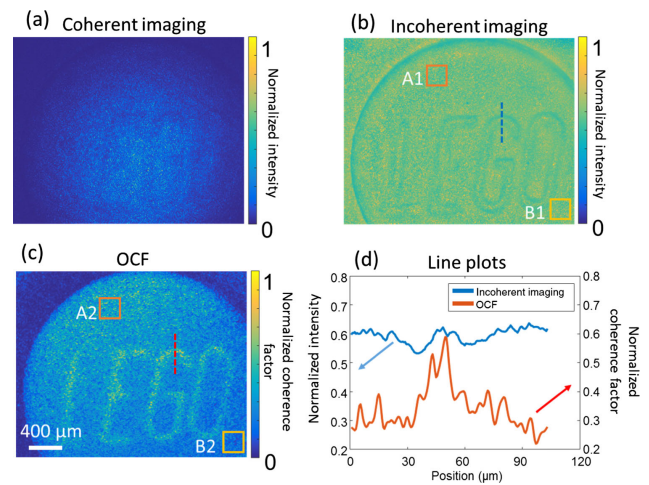


Fig. 5. Comparison on different imaging modalities. (a) Coherent imaging. (b) Incoherent imaging. (c) OCF. (d) Line plots of blue and red dashed lines in (b) and (c). The mean values in A1 and B1 are 0.59 and 0.60, respectively. The mean values in A2 and B2 are 0.38 and 0.17, respectively.

We then used OCF to image the 3D-printed samples (3D printer model number CraftUnique CraftBot Plus) with a given printing resolution of 100 μm [Figs. 4(b) and 4(c)]. In Fig. 4(b3), the 100 μm step is clearly seen in the line plot. Figure 4(c) illustrates the imaging results of a 3D-printed hand model.

Using the same imaging system, we then imaged the same test objects with different imaging modalities, showing that OCF provides a different imaging contrast mechanism in comparison to conventional coherent or incoherent imaging. Figures 5(a)–5(c) show the imaging results of coherent imaging, incoherent imaging, and OCF, respectively. Speckle noise is dominant in coherent imaging and can overwhelm the features of the sample. Both incoherent imaging and OCF are able to reveal the feature information of the sample. In the incoherent imaging, the intensity values are uniform among the FoV, but relatively lower at the edges of the test object as more light is scattered. Unlike incoherent imaging, OCF maps the coherence factor that is related to the height instead of feature edges, since different height provides different pathlength mismatch and yields different fringe visibility in the hologram. In Fig. 5(d), we show the line plots indicated by the blue and red lines in Figs. 5(b) and 5(c), respectively. OCF imaging is directly tied to the height itself since different heights result in different coherence factors, while incoherent imaging reveals the edge information of the feature (the feature has a similar intensity value as the surrounded background, with two dips at the edge of the feature). Furthermore, the sample is put slightly tilted, thus the surface is not perpendicular to the optical axis. From OCF, the tilt is shown by different fringe visibility in enclosed square A1 (mean value 0.38) and square B1 (mean value 0.17), while the absolute intensity values (reflectance) in enclosed squares A2 (mean value 0.59) and B2 (mean value 0.60) are similar from incoherent imaging.

As a 3D imaging method, OCF has several advantages over other 3D imaging methods. While OCF and OCT both use interference to determine height information, the mechanism by which they do so are quite different. OCT uses light with

optical coherence lengths that are much shorter than the DoF. Therefore, to get the height measurement within the DoF, either time domain or frequency domain sweeping is required, and multiple 2D images are used to calculate one 3D image, which requires longer data acquisition time and more computational resources. On the other hand, OCF uses light with coherence lengths that are comparable to the DoF, and uses the strength of the interference to determine height information. Thus, the entire scene within the DoF can interfere with the reference beam to varying extents, and the height information is encoded in a single OCF interference hologram. Compared to structured illumination, besides single-shot advantage, OCF does not have to address the phase wrapping problem, to which many efforts have been devoted. In terms of space-bandwidth product (SBP) of the imaging system, OCF does not require as such binning of the camera pixels into image pixels as light field imaging requires. As seen from Fig. 3 ($F\{I(\mathbf{r})\}$), the two enclosed red circles, which represent the pass band on Fourier domain, occupy $\sim 16\%$ of the total Fourier space. This implies that $\sim 16\%$ of the total pixels are effectively used. Unlike lensless cameras or PSF engineering 3D based imaging, which adopt a variety of mathematical models and computational algorithms, OCF is more computationally efficient since it only requires a single 2D Fourier transform.

In our experiment, the coherence length of the light source is ~ 2 mm, which is similar to the DoF of the imaging system. However, the principle of OCF can be applied to measure a broader range of heights, from microns to meters, by the selection of a light source with a suitable coherence length. The imaging system can then be designed accordingly.

In conclusion, we demonstrate single-shot 3D surface imaging using OCF. The experimental results suggest that it is viable for quantitative height measurement. Using the same imaging system, we also show that OCF has a different imaging contrast mechanism than conventional imaging modalities, including coherent imaging and incoherent imaging. The contrast mechanism of OCF is able to reveal some information that is not provided by the conventional imaging modalities.

The use of OCF offers a simple and effective solution for surface profile reconstruction and may have potential applications for industrial quality control inspection due to its single-shot property.

Funding. Donna and Benjamin M. Rosen Bioengineering Center, California Institute of Technology (9900050).

Acknowledgment. We thank Cheng Shen and Dr. Yan Liu for their help with sample preparation, and Dr. Baptiste Blochet for helpful discussions.

Disclosures. The authors declare no conflicts of interest.

REFERENCES

1. D. Huang, E. A. Swanson, C. P. Lin, J. S. Schuman, W. G. Stinson, W. Chang, M. R. Hee, T. Flotire, K. Gregory, C. A. Puliafito, and J. G. Fujimoto, *Science* **254**, 1178 (1991).
2. Z. Wang, B. Potsaid, L. Chen, C. Doerr, H.-C. Lee, T. Nielson, V. Jayaraman, A. E. Cable, E. Swanson, and J. G. Fujimoto, *Optica* **3**, 1496 (2016).
3. J. Geng, *Adv. Opt. Photon.* **3**, 128 (2011).
4. R. Ng, M. Levoy, M. Bredif, G. Duval, M. Horowitz, and P. Hanrahan, "Light field photography with a hand-held plenoptic camera," Technical Report CTSR 2005-02 (Stanford University, 2005).
5. M. Levoy, R. Ng, A. Adams, M. Footer, and M. Horowitz, *ACM SIGGRAPH* (2006), pp. 924–934.
6. N. Antipa, G. Kuo, R. Heckel, B. Mildenhall, E. Bostan, R. Ng, and L. Waller, *Optica* **5**, 1 (2018).
7. M. S. Asif, A. Ayremlou, A. Veeraraghavan, R. Baraniuk, and A. Sankaranarayanan, *IEEE International Conference on Computer Vision* (2016), Vol. **2016**, pp. 663–666.
8. A. Levin, R. Fergus, F. Durand, and W. T. Freeman, *ACM SIGGRAPH Conference on Computer Graphics* (2007).
9. S. R. P. Pavani, M. A. Thompson, J. S. Biteen, S. J. Lord, N. Liu, R. J. Twieg, R. Piestun, and W. E. Moerner, *Proc. Natl. Acad. Sci. USA* **106**, 2995 (2009).
10. P. Lull, X. Yuan, L. Carin, and D. J. Brady, *Optica* **2**, 822 (2015).
11. M. Takeda, H. Ina, and S. Kobayashi, *J. Opt. Soc. Am.* **72**, 156 (1982).